Biochemistry-Enabled 3D Foams for Ultrafast Battery Cathodes

Yanping Zhou,[‡,§,#] Xianhong Rui,[†,‡,#] Wenping Sun,[‡] Zhichuan Xu,[‡] Yan Zhou,[§,⊥] Wun Jern Ng,[§,⊥] Qingyu Yan,[*,‡] and Eileen Fong[*,‡]

[†]School of Energy and Environment, Anhui University of Technology, Maanshan, Anhui 243002, China, [‡]School of Materials Science and Engineering and [⊥]School of Civil and Environmental Engineering, Nanyang Technological University, 639798, Singapore, and [§]Advanced Environmental Biotechnology Centre, Nanyang Environment and Water Research Institute, Nanyang Technological University, 1 CleanTech Loop, 637141, Singapore. [#]Yanping Zhou and Xianhong Rui contributed equally to this work.

ABSTRACT Metal vanadium phosphates (MVP), particularly $Li_3V_2(PO_4)_3$ (LVP) and $Na_3V_2(PO_4)_3$ (NVP), are regarded as the next-generation cathode materials in lithium/sodium ion batteries. These materials possess desirable properties such as high stability, theoretical capacity, and operating voltages. Yet, low electrical/ionic conductivities of LVP and NVP have limited their applications in demanding devices such as electric vehicles. In this work, a novel synthesis route for the preparation of LVP/NVP micro/mesoporous 3D foams *via* assembly of elastin-like polypeptides is demonstrated. The as-synthesized MVP 3D foams consist of microporous networks of mesoporous nanofibers, where the surfaces of individual fibers are covered with MVP nanocrystallites. TEM images further reveal that LVP/NVP nanoparticles are about 100–200 nm in diameter, with each particle enveloped by a 5 nm thick carbon shell. The MVP 3D foams prepared in this work exhibit ultrafast rate capabilities (79 mA h g^{-1} at 100C and 66 mA h g^{-1} at 200C for LVP 3D foams; 73 mA h g^{-1} at 100C and 51 mA h g^{-1} at 200C for NVP 3D foams) and excellent cycle performance (almost 100% performance retention after 1000 cycles at 100C); their properties are far superior compared to current state-of-the-art active materials.

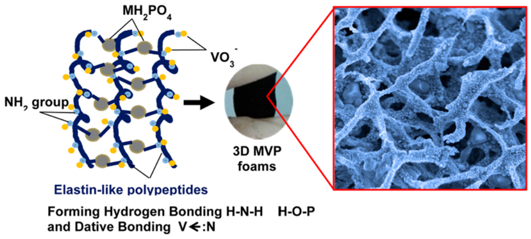

KEYWORDS: metal vanadium phosphates · lithium ion battery · sodium ion battery · elastin-like polypeptides · 3D nanostructures

Three-dimensional (3D) hierarchical foam nanoarchitectures have recently attracted significant attention for lithium/sodium energy storage applications by offering sufficient contact area between the electrolyte and electrode, high-rate transportation of ions and electrons, and short solid-state ion diffusion lengths. These properties favor the use of 3D foam nanomaterials in advanced plug-in hybrid vehicles (PHEVs) and electric vehicles (EVs) with rapid charge and discharge requirements.[1−3] In the field, intensive research effort has been devoted to the fabrication of numerous 3D structured battery anodes, such as Cu_6Sn_5 alloy foams,[4] Ni-foam-supported CoO-Li_2O,[5] Fe_3O_4/graphene foams,[6−8] and MoS_2/graphene foams.[9] Current strategies used for the preparation of such 3D foams include hydrothermal self-assembly, template-assisted preparation, electrostatic spray deposition, chemical vapor deposition (CVD), and atomic layer deposition (ALD). However, it is difficult to use these conventional approaches to produce 3D foam cathodes, particularly cathode materials with complex stoichiometric compositions.

Biological molecules and organisms (*e.g.*, polysaccharides, proteins, viruses, DNA, peptides) have been employed to synthesize nanomaterials due to their environmentally friendly synthesis conditions. More importantly, it is possible to genetically engineer molecules to interact with metallic precursors under benign conditions and to create inorganic nanostructures with high surface areas, with precise control over their compositions, phase, shape, and size.[10−14] For example, peptides, phages, viruses, and proteins have been successfully used to guide the formation of FePt,[15] Co_3O_4,[16] and iron oxide nanoparticles (NPs),[17] $BaTiO_3$ NPs,[18] Co_3O_4 nanowires,[19] $FePO_4$ nanofibers,[20] and so on. Most of these systems focused on preparing naturally 0D or 1D nanostructures; construction of more complex inorganic

* Address correspondence to
alexyan@ntu.edu.sg,
wmfong@ntu.edu.sg.

Received for review February 9, 2015
and accepted April 10, 2015.

10.1021/acsnano.5b00932

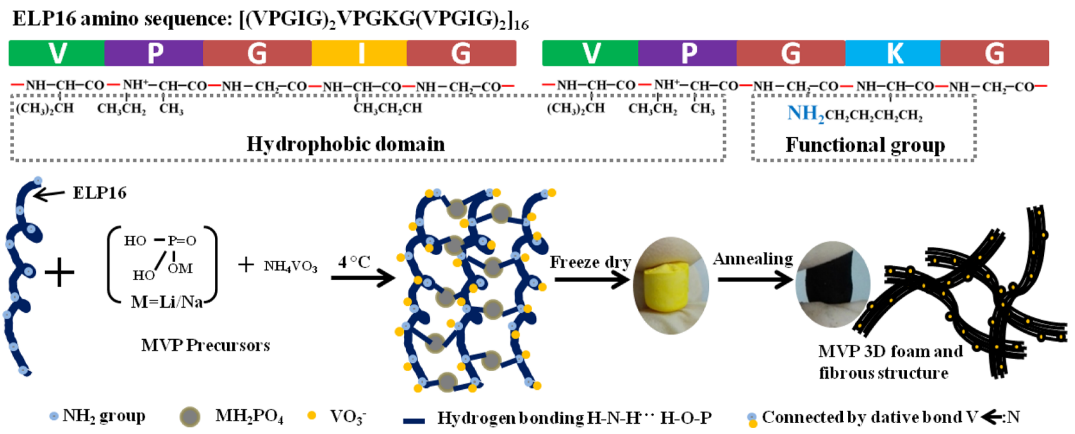

Scheme 1. Schematic Illustrating the Mechanisms in the Synthesis of MVP 3D Foams Using Recombinant ELP16 Proteins

materials and architectures (*e.g.*, 3D foams) *via* biological routes has not been demonstrated.

Metal vanadium phosphates (MVP), particularly $Li_3V_2(PO_4)_3$ (LVP) and $Na_3V_2(PO_4)_3$ (NVP) NPs, are promising cathode materials for lithium ion batteries and sodium ion batteries due to their excellent thermal stabilities, large reversible capacities, high operating potentials, and relatively rapid ionic mobilities. Currently, LVP and NVP are manufactured at the micro- or submicroscales using traditional energy-intensive solid-state ceramic processes.[21−25] In this work, we demonstrate a facile strategy for the preparation of LVP and NVP nanostructures supported on hierarchically porous 3D carbon aerogels using recombinant elastin-like polypeptides. Elastin-like polypeptides (ELPs) are known to undergo self-aggregation through a temperature-induced coacervation process and are widely studied for a wide variety of applications including tissue engineering and bioremediation.[26] Here, we designed and prepared a recombinant protein, ELP16 with an amino acid sequence of $[(VPGIG)_2VPGKG(VPGIG)_2]_{16}$, containing repetitive valine, proline, glycine, isoleucine, and lysine amino acid sequences, to direct the growth of LVP and NVP particles. Scheme 1 illustrates the steps involved in the synthesis. The lysine (K) residues incorporated periodically within the elastin framework provide amine side groups that interact with $H_2PO_4^-$ and VO_3^- ions through hydrogen bonding and/or dative bonding. These interactions serve as "cross-links" between two adjacent ELP16 molecules, causing the formation of ELP16 fibers. During annealing, the N atoms combine both phosphates and vanadium and act as nucleating centers for the formation of LVP or NVP nanoparticles. Meanwhile, ELP16 is degraded into carbon matter, resulting in carbon-enveloped LVP or NVP NPs dispersed within a 3D conductive carbon aerogel network. The as-synthesized 3D MVP nanostructures show ultrahigh capacities with ultrafast charging/discharging properties and excellent cycle performances as cathodes for Li/Na secondary batteries.

RESULTS AND DISCUSSION

The recombinant ELP16 proteins were readily purified by inverse temperature cycling to yield 1 g of lyophilized product per 9 L of culture. ELP16 and soluble MVP precursors were mixed on ice to avoid unwanted precipitation of ELP16 proteins.[27] The mixture was then freeze-dried and annealed to obtain the 3D foam-like structures as shown in Figure 1. From the XRD spectrum of the as-annealed sample (see Supporting Information, Figure S1A), characteristic peaks of well-crystallized $Li_3V_2(PO_4)_3$ (JCPDF no. 04-012-2044) could be seen. The Al peak was from the sample holder. There are no detectable impurity phases, indicating that we had successfully obtained pure crystalline $Li_3V_2(PO_4)_3$. Figure 1A shows the field-emission scanning electron microscope (FESEM) image of the as-synthesized 3D LVP foam (abbreviated as LVP@C/CAs). From the image, it was clear that the annealed product consisted of a nanofibrous porous network structure. FESEM images at a higher magnification (Figure 1B) also revealed that the micropores were around 3 μm in diameter. The surfaces of the nanofibers were completely covered by LVP nanoparticles (Figure 1C). A transmission electron microscope (TEM) image at low magnification (see Supporting Information, Figures S2A) shows the interconnected fibrous carbon matrix, confirming the formation of the aerogel structure. Figure 1D shows the TEM image of the nanofibers. LVP nanoparticles with diameters of about 100−200 nm were found to be embedded within the carbon matrix. Under higher magnifications (Figure 1E), it was clear that the LVP nanoparticles were encased by an amorphous carbon shell of around 5 nm thick, with the observed lattice spacing of 3.65 Å corresponding to the (211) plane of LVP. The carbon shell was probably from the pyrolysis of ELP16. The ELP16 scaffold was degraded into carbon matter during the annealing step, resulting in the carbon coating outside LVP nanoparticles and formation of a 3D conductive carbon porous matrix. This carbon matrix allowed the LVP

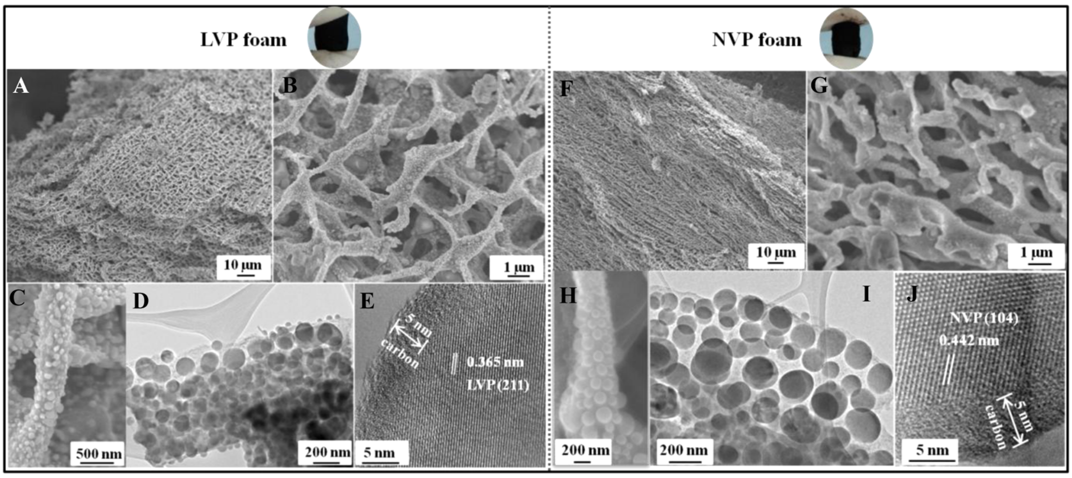

Figure 1. (A–C) FESEM images of as-synthesized LVP 3D foams at various magnifications; (D) TEM image showing LVP nanoparticles embedded within a carbon matrix; (E) measured lattice spacing (0.367 nm) corresponding to the (211) plane of LVP; (F–H) FESEM images of as-synthesized NVP 3D foams at various magnifications; (I) TEM image confirming NVP nanoparticles embedded within a carbon matrix; (J) measured lattice spacing (0.442 nm) corresponding to the (104) plane of NVP.

nanoparticles to nucleate and grow at high temperatures without aggregation. The overall carbon content derived from the recombinant ELP16 matter was determined by dissolving the as-synthesized product in hot concentrated HCl and weighing the residual carbon. It was found that it contained about 22 wt % carbon. BET results of the product (see Supporting Information, Figure S3A) indicated that a large amount of mesopores existed within the fibrous carbon matrix, with a specific surface area of 106.3 m^2 g^{-1} and a narrow pore size distribution centered at 4 nm. Here, we conclude that hierachically micro/mesoporous LVP@C/CAs nanostructures were indeed obtained.

To demonstrate the generality of our approach, we applied the same synthesis procedure to yield 3D NVP foams (abbreviated as NVP@C/CAs). The XRD results (see Supporting Information, Figure S1B) indicated that pure crystallized $Na_3V_2(PO_4)_3$ (JCPDF no. 96-222-5133) was indeed obtained. Figure 1F–H show the FESEM images of the annealed NVP 3D foams. The morphologies of the foams were similar to that of the LVP@C/CAs 3D foams shown in Figure 1A–C. The NVP 3D foams also consisted of a nanofibrous microporous network, covered by NVP nanoparticles. TEM images at low magnification (see Supporting Information, Figure S2B) also show similar aerogel structures found in LVP@C/CAs. Figure 1I is a TEM image of the fibers, clearly showing the presence of NVP nanocrystallites embedded within a carbon matrix. The NVP nanopaticles with diameters less than 200 nm were also encased by an amorphous carbon shell of around 5 nm thick, with the measured lattice spacing of 4.42 Å corresponding to the (104) plane of NVP (Figure 1J). BET results (see Supporting Information, Figure S3B) indicated that the specific surface area of NVP@C/CAs is 131.9 m^2 g^{-1} and the pore size distribution is centered at 3 nm. Here, we demonstrated that micro/mesoporous NVP@C/CAs nanostructures could also be successfully fabricated *via* the same strategy.

To understand the mechanisms involved in the synthesis process, four separate mixtures containing (1) ELP16 and both precursors, (2) ELP16 and LiH_2PO_4, (3) ELP16 and NH_4VO_3, and (4) ELP16 only were prepared at 4 °C and freeze-dried. Samples were immediately examined under FESEM. For ELP16 and both precursors, ELP16/LiH_2PO_4 and ELP16/NH_4VO_3 mixtures, fibrous porous structures were obtained (Figure 2A–C). However, in the absence of either LiH_2PO_4 or NH_4VO_3, we were unable to obtain any nanofibers (see Supporting Information, Figure S4A). Instead, the sample collapsed into a fine powder after annealing. Taken together, it is likely that interactions between LiH_2PO_4, NH_4VO_3, and ELP16 facilitated the formation of the nanofibrous network. Our FTIR results shown in Figure 2C revealed shifts in the characteristic peaks for P–O stretching (*i.e.*, from 1079 to 1050 cm^{-1}) and V–O–V stretching (from 942 to 967 cm^{-1}) when LVP precursors were mixed with ELP16.[28,29] Both results suggest that there were indeed interactions between $H_2PO_4^-$ ions and ELP16 as well as between VO_3^- ions and ELP16. In addition, there were also shifts in peaks for C–NH_2 stretching (from 1234 to 1260 cm^{-1}).[30] Therefore, the interactions between $H_2PO_4^-$ ions and ELP16 were likely due to hydrogen bonding between P–O–H and H–N–H, since there are 16 lysine residues (and hence 16 amine groups) per ELP16 molecule (Scheme 1). The hydrogen bonding reduced the polarity of the P–O bond and resulted in the shifts of P–O stretching peaks. On the other hand, interactions between VO_3^- ions and ELP16 could be due to the formation of dative bonds from the vacant electron orbits of VO_3^- and the lone pairs of the –NH_2 on ELP16. Both interactions contributed to the shift in the characteristic peaks for C–NH_2 stretching to higher

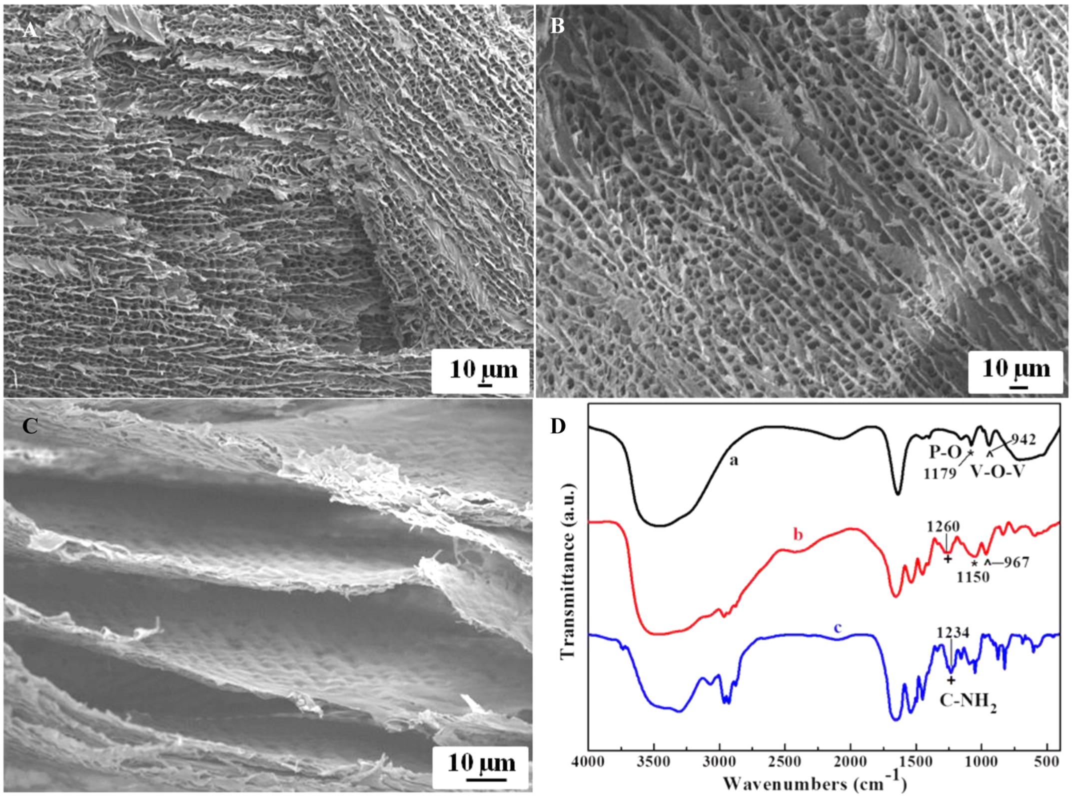

Figure 2. FESEM images of (A) ELP16, LiH_2PO_4, and NH_4VO_3, (B) ELP16 and LiH_2PO_4, and (C) ELP16 and NH_4VO_3 mixtures obtained after freeze-drying; (D) FTIR spectra of LVP precursors only (curve a), ELP16 + LVP precursors (curve b), and ELP16 only (curve c). The shifts in P−O stretching, V−O−V stretching, and C−NH_2 stretching peaks are indicated.

wavenumbers by increasing the polarity of the C−N bond. Therefore, the possible mechanisms involved are proposed as follows. In pure ELP16 solutions, there exists hydrophobic forces stemming from the presence of hydrophobic residues along the ELP16 backbone (Scheme 1). These hydrophobic forces coacervate the ELP16 molecules together. Meanwhile, an electrostatic repulsion force also exists between dissociated $-NH_2$ groups on the lysine residues. This electrostatic repulsion force acts to disperse the ELP16 molecules. When both forces cancel each other (as in the case of ELP16 only mixtures), nanofibers could not be formed. However, when LVP or NVP precursors are present, $H_2PO_4^-$ and/or VO_3^- ions could bind to the $-NH_2$ groups in ELP16 and act as cross-linkers between two adjacent ELP16 molecules. These interactions are further strengthened by the formation of hydrogen bonding and/or dative bonding, thereby enhancing the association of adjacent ELP16 molecules while reducing the dispersive effects of the electrostatic repulsion. Hence, interactions between the $H_2PO_4^-$ and VO_3^- ions and ELP16 drive the formation of ELP16 bundles. In addition, the recruitment of $H_2PO_4^-$ and VO_3^- ions on the ELP16 backbone also contributed to an overall negative charge on the surface of the ELP16 bundles and further facilitated the recruitment of M^+ ions. We also noted that the freeze-drying step was critical to preserve the integrity of the structure, without which the micropore network could not be maintained (see Supporting Information, Figure S4B).

The electrochemical performance of MVP 3D foams was examined by galvanostatic cycling in CR2032 coin-type cells. Metallic lithium and sodium foils were used as the counter electrodes for LVP and NVP cathodes, respectively. Figure 3A,B show the initial charge−discharge voltage characteristics of the LVP and NVP cathodes at a rate of 1C, respectively. Insets in Figure 3A,B are their corresponding cycling performances. A rate of *n*C corresponds to a full charge or discharge in 1/*n* hour. Here, 1C equals the current density of 133 mA g^{-1} for LVP and 118 mA g^{-1} for NVP, respectively. The redox plateau potentials of V^{3+}/V^{4+} are clearly observed at around 3.6, 3.7, and 4.1 V (*vs* Li^+/Li) for LVP and ∼3.4 V (*vs* Na^+/Na) for NVP, corresponding to two lithium or sodium extraction/insertion, *i.e.*, $M_3V_2(PO_4)_3 \leftrightarrow MV_2(PO_4)_3$ (M = Li and Na). The potential hysteresis was found to be less than 0.06 V, thereby implying an excellent reversibility for Li/Na ion removal and uptake. As a result, at 1C, initial discharge capacities of up to 129 and 112 mA h g^{-1} with Coulombic efficiencies (calculated from the discharge capacity/charge capacity) of 98% and 97% were achieved for LVP and NVP cathodes, respectively. Both efficiencies were nearly equivalent to their theoretical values. It was noted here that the capacity contribution

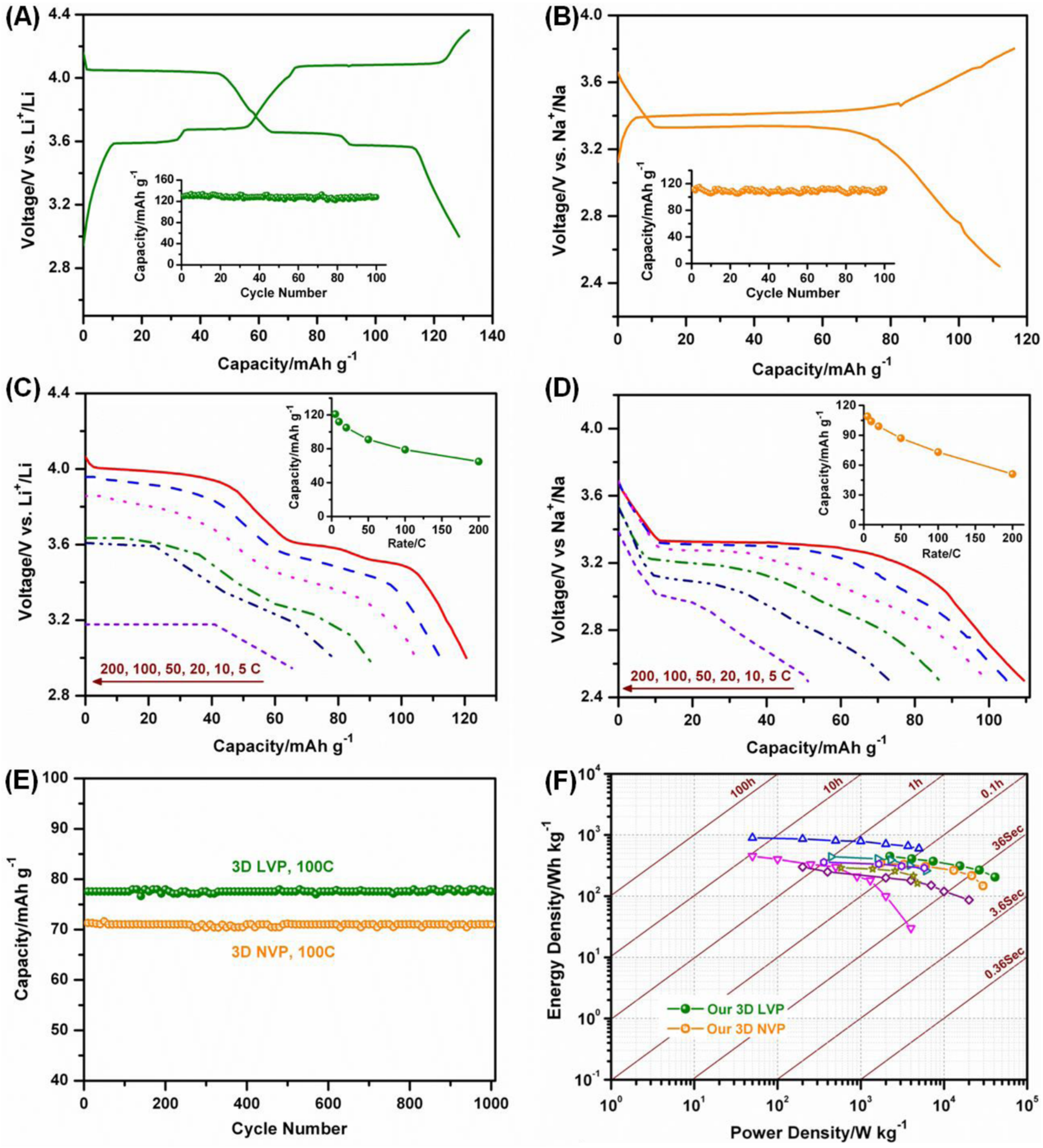

Figure 3. Initial charge−discharge voltage profiles of (A) LVP and (B) NVP cathodes at 1C. Insets show the corresponding cycling performances for each material. Galvanostatic discharging profiles of (C) LVP and (D) NVP cathodes at current rates of 5C to 200C (their discharge capacities *vs* C rates are summarized in the insets). (E) Cycling stability of LVP and NVP at 100C. (F) Ragone plots of our 3D MVP cathodes, compared with some advanced active materials of $LiNi0.5Mn0.5O_2$ (up triangles), CNT/$FePO_4$ nanowires (down triangles), $LiFePO_4$/C (diamonds), LVP/C thin film (right triangles), $Na_3Ni_2SbO_6$ (hexagons), and NVP/graphene (stars).

from the carbon is negligible in the voltage ranges of 3.0−4.3 V (*vs* Li^+/Li) and 2.5−3.8 V (*vs* Na^+/Na), and hence, only the masses of active LVP and NVP were included when calculating the specific capacities. In addition, a near perfect capacity retention (∼99.5%) was observed for both types of cathodes during 100 cycles (insets in Figure 3A,B).

The key advantage of our 3D MVP cathodes is their excellent ultrafast charging/discharging performances, which are highly desirable for high-power LIB/NIB applications such as HEVs and EVs. The discharge voltage profiles of LVP and NVP obtained at discharge rates from 5C to 200C are shown in Figure 3C and D, respectively. The discharge capacities of LVP were found to be 121, 112, 105, 91, and 79 mA h g^{-1} at discharge rates of 5, 10, 20, 50, and 100C (Figure 3C). More significantly, the LVP 3D foam cathodes were able to achieve a capacity of 66 mA h g^{-1} (∼50% of its theoretical capacity), even at an ultrahigh rate of 200C (which corresponded to a time of 18 s to fully discharge). This performance is nearly 1 order of magnitude larger than materials used in current battery cathodes. Likewise, the 3D NVP cathodes were also able to deliver reversible capacities of 109, 104, 99, 87, 73, and 51 mA h g^{-1} at rates of 5, 10, 20, 50, 100, and 200C (Figure 3D). Both materials synthesized in this work demonstrated ultrafast discharging properties, far superior to most state-of-the-art LVP and NVP cathodes reported in the literature (see Supporting Information, Tables S1 and S2). Our MVP cathodes also exhibit outstanding long-term high rate cycling performances. From Figure 3E, there were no obvious capacity losses for LVP and NVP cathodes over 1000 cycles at a rate of 100C.

Finally, to evaluate the possible applications of our LVP and NVP 3D foams as cathode materials, we calculated their power and energy densities based on the weight of cathode materials, working voltages, and capacities at various rates. Figure 3F shows the Ragone plot for our materials, compared to current advanced LIB and NIB cathodes (normalized to the weight of cathode materials). The LVP cathodes prepared in this work were able to achieve a specific energy density of 450 Wh kg^{-1} at a power density of 2.2 kW kg^{-1}, while maintaining an energy density of 205 Wh kg^{-1} at an ultrahigh power density of 41 kW kg^{-1}. Similarly, the NVP cathodes prepared in this work were able to achieve gravimetric energies of 350 and 147 Wh kg^{-1} at specific powers of 1.8 and 30 kW kg^{-1}, respectively. Notably, the maximum specific power densities achieved by our MVP cathodes are significantly higher than the current state-of-the-art active materials such as $LiNi_{0.5}Mn_{0.5}O_2$,[31] CNT/$FePO_4$ nanowires,[20] $LiFePO_4$/C,[32] LVP/C thin film,[33] $Na_3Ni_2SbO_6$,[34] and NVP/graphene.[35] Hence, we envisioned that the LVP and NVP 3D foams developed in this work have tremendous potential for use in demanding energy storage applications such as HEVs and EVs.

Plausible mechanisms enabling ultrafast charge/discharge properties of 3D LVP and NVP cathodes are illustrated as below. (i) It is well known that nanoscale materials have exceptionally short ion (Li^+ and Na^+) transport lengths, leading to a short time constant t for ion diffusion. Taking the estimated values of ion diffusivity D ($\sim 10^{-10}$ cm^2 s^{-1} for LVP and $\sim 10^{-11}$ cm^2 s^{-1} for NVP),[36,37] the time t for Li^+ and Na^+ to diffuse over 100 nm (average particle size, L) is estimated to be 1 and 10 s for LVP and NVP, respectively, computed using the equation $t = L^2/D$. Thus, the limiting factor in the improvement of the charge/discharge rate is the delivery of ions and electrons to the surface of our monodispersed LVP and NVP nanoparticles rather than solid-state ion transport. (ii) The large surface area of electrodes (106.3 m^2 g^{-1} for LVP@C/CAs, 131.9 m^2 g^{-1} for NVP@C/CAs) permits a high contact area with the electrolytes (see Supporting Information Figure S2 for BET measurements). (iii) The 3D interconnected electrolyte-filled pore networks provide a fast transport channels for the conductive ions. (iv) The 3D nanoporous carbon monolith combined with the carbon coating on the nanocrystals can further act as the electrolyte reservoir and as the electronic conductor. The carbon matrix allows fast migration of both Li^+/Na^+ and e^- to the active sites of each LVP/NVP nanoparticle. Therefore, favorable transport characteristics of the unique hierarchical structure with an efficiently mixed conducting 3D network are assumed to lead to the overall excellent power performance.

CONCLUSIONS

Metal vanadium phosphates have been explored as promising materials for cathodes in metal ion batteries. However, their low conductitivies limit their widespread use in applications where ultrahigh power capabilities are required, without significant loss in energy over time. In this work, we report a novel synthesis approach to prepare nanostructured MVP 3D foams *via* assembly of recombinant elastin-like polypeptides (ELP16) proteins. We showed that we were able to obtain 3D fibrous, macroporous LVP and NVP foams that displayed exceptional rate cycling capabilities and energy densities, far superior to current advanced active materials used for state-of-the-art battery technologies.

METHODS

Expression and Purification of ELP16. The plasmid pET22b containing the gene encoding for ELP16 was constructed by modifying a previously reported construct.[38] Bacteria BL21-(DE3)pLysS cells were transformed with pET22b plasmid encoding the ELP16 gene *via* heat shock. Colonies were selected and grown in 50 mL of TB (Terrific broth) media containing 50 mg L^{-1} ampicillin and 34 mg L^{-1} chloramphenicol overnight. The next day, 10 mL of bacteria culture was reinoculated into 1 L of TB media containing the same antibiotics and grown to an optical density at 600 nm (OD_{600}) of 0.7−0.8 at 37 °C. To induce protein expression, isopropyl β-D-1-thiogalactopyranoside (IPTG) was added to a final concentration of 1 mM. Bacterial cells were harvested after 4 h by centrifugation at 8000 rpm at 4 °C for 20 min before resuspending in TEN buffer (0.1 M Tris, 0.01 M EDTA, 1 M NaCl). The cell mixture was sonicated on ice and subsequently centrifuged at 4 °C to collect the supernatant. The ELP16 was purified *via* inverse thermal cycling as previously described.[38] Purified ELP16 was dialyzed against water for 3 days and lyophilized. Lyophilized ELP16 proteins were store at −20 °C for further use.

Synthesis of LVP/NVP 3D Porous Nanostructures. Purified ELP16 was dissolved in cold dH_2O. Soluble precursors LiH_2PO_4/NaH_2PO_4 and NH_4VO_3 were dissolved in 60 °C dH_2O with stirring to achieve a concentration of 0.3 and 0.2 M, respectively. The LVP/NVP precursors were cooled on ice and added to the ELP16 solution with vigorous stirring on ice. The final concentration of ELP16 in the mixture was 7.5 wt %/vol, and 125 mM and 187.5 mM for NH_4VO_3 and MH_2PO_4 respectively. The mixture was then kept stagnant for 1 h and subsequently frozen in liquid nitrogen before lyophilization. The resulting sample was annealed at 750 °C for 10 h under an argon atmosphere. Minute amounts of HNO_3 acid were added to the NVP precursors solution before mixing with ELP16 to avoid precipitation at low temperature.

Materials Characterization. Powder X-ray diffraction (XRD, Shimadzu powder) was performed using Cu Kα_a radiation to identify the crystalline phases of the synthesized materials. The morphologies and particle sizes were determined by analyzing images acquired by FESEM and TEM. FESEM images were taken using a JEOL model JSM-7600F. TEM images were acquired using a JEOL 2010F TEM operated at an accelerating voltage of 200 kV. FT-IR spectra were recorded on a Fourier transform infrared spectrometer (PerkinElmer) with a DGTS detector. Nitrogen adsorption/desorption isotherms were conducted at 77 K (ASAP 2020).

Electrochemical Measurements. The coin-type cells were assembled in an argon-filled glovebox, where both moisture and oxygen levels were less than 1 ppm. The electrodes were fabricated by mixing 80 wt % LVP or NVP with carbon nanotube (10 wt %) and polyvinylidene fluoride (PVDF, 10 wt %) in *n*-methyl-2-pyrrolidone solvent and then pasted onto the aluminum foils. The mass loading in electrodes was around 1.0 mg cm^{-2}. For LVP LIB cells, lithium foils were used as anodes and the electrolyte solution was made of 1 M $LiPF_6$ in ethylene carbonate/diethyl carbonate (1/1, w/w). For NVP NIB cells, sodium foils were used as anodes and the electrolyte solution was made of 1 M $NaClO_4$ in propylene carbonate with 5% fluoroethylene carbonate. All cells were tested on a NEWARE multichannel battery test system with galvanostatic charge and discharge in the voltage ranges of 3.0−4.3 V *vs* Li^+/Li for LVP and 2.5−3.8 V *vs* Na^+/Na for NVP.

Conflict of Interest: The authors declare no competing financial interest.

Acknowledgment. The authors acknowledge funding from Nanyang Technological University, Singapore. Yanping Zhou is supported by an IGS-NEWRI scholarship. Q. Yan gratefully acknowledges Singapore MOE AcRF Tier 1 grants RG2/13 and Singapore National Research Foundation under the CREATE program EMobility in Megacities. X. Rui gratefully acknowledges the program of the Leading Talent Team in Universities of Anhui Province, China. The characterization work was performed at the Facility for Analysis, Characterization, Testing and Simulation in Nanyang Technological University.

Supporting Information Available: Chemical physical characterizations (XRD patterns and nitrogen adsorption/desorption isotherms) for as-synthesized 3D LVP foam and 3D NVP foam; FESEM image of 7.5% ELP solution after freeze-drying and FESEM image of ELP16+ LVP precursor solution placed at room temperature for 1 h, followed by freeze-drying; an electrochemical performance comparison of our products to previously reported LVP/NVP cathodes. This material is available free of charge *via* the Internet at http://pubs.acs.org.

REFERENCES AND NOTES

1. Long, J. W.; Dunn, B.; Rolison, D. R.; White, H. S. Three-Dimensional Battery Architectures. *Chem. Rev.* **2004**, *104*, 4463–4492.
2. Jiang, L.; Fan, Z. Design of Advanced Porous Graphene Materials: From Graphene Nanomesh to 3D Architectures. *Nanoscale* **2014**, *6*, 1922–1945.
3. Chabi, S.; Peng, C.; Hu, D.; Zhu, Y. Ideal Three-Dimensional Electrode Structures for Electrochemical Energy Storage. *Adv. Mater.* **2014**, *26*, 2440–2445.
4. Shin, H. C.; Liu, M. Three-Dimensional Porous Copper−Tin Alloy Electrodes for Rechargeable Lithium Batteries. *Adv. Funct. Mater.* **2005**, *15*, 582–586.
5. Yu, Y.; Chen, C. H.; Shui, J. L.; Xie, S. Nickel-Foam-Supported Reticular CoO−Li_2O Composite Anode Materials for Lithium Ion Batteries. *Angew. Chem., Int. Ed.* **2005**, *44*, 7085–7089.
6. Wei, W.; Yang, S.; Zhou, H.; Lieberwirth, I.; Feng, X.; Müllen, K. 3D Graphene Foams Cross-Linked with Pre-Encapsulated Fe_3O_4 Nanospheres for Enhanced Lithium Storage. *Adv. Mater.* **2013**, *25*, 2909–2914.
7. Luo, J.; Liu, J.; Zeng, Z.; Ng, C. F.; Ma, L.; Zhang, H.; Lin, J.; Shen, Z.; Fan, H. J. Three-Dimensional Graphene Foam Supported Fe_3O_4 Lithium Battery Anodes with Long Cycle Life and High Rate Capability. *Nano Lett.* **2013**, *13*, 6136–6143.
8. Chen, W.; Li, S.; Chen, C.; Yan, L. Self-Assembly and Embedding of Nanoparticles by *in Situ* Reduced Graphene for Preparation of a 3D Graphene/Nanoparticle Aerogel. *Adv. Mater.* **2011**, *23*, 5679–5683.
9. Gong, Y.; Yang, S.; Liu, Z.; Ma, L.; Vajtai, R.; Ajayan, P. M. Graphene-Network-Backboned Architectures for High-Performance Lithium Storage. *Adv. Mater.* **2013**, *25*, 3979–3984.
10. Nam, Y. S.; Magyar, A. P.; Lee, D.; Kim, J.-W.; Yun, D. S.; Park, H.; Pollom, T. S.; Weitz, D. A.; Belcher, A. M. Biologically Templated Photocatalytic Nanostructures for Sustained Light-Driven Water Oxidation. *Nat. Nanotechnol.* **2010**, *5*, 340–344.
11. Royston, E.; Ghosh, A.; Kofinas, P.; Harris, M. T.; Culver, J. N. Self-Assembly of Virus-Structured High Surface Area Nanomaterials and Their Application as Battery Electrodes. *Langmuir* **2008**, *24*, 906–912.
12. Chen, C. L.; Rosi, N. L. Peptide-Based Methods for the Preparation of Nanostructured Inorganic Materials. *Angew. Chem., Int. Ed.* **2010**, *49*, 1924–1942.
13. Uchida, M.; Klem, M. T.; Allen, M.; Suci, P.; Flenniken, M.; Gillitzer, E.; Varpness, Z.; Liepold, L. O.; Young, M.; Douglas, T. Biological Containers: Protein Cages as Multifunctional Nanoplatforms. *Adv. Mater.* **2007**, *19*, 1025–1042.
14. Dickerson, M. B.; Sandhage, K. H.; Naik, R. R. Protein- and Peptide-Directed Syntheses of Inorganic Materials. *Chem. Rev.* **2008**, *108*, 4935–4978.
15. Reiss, B. D.; Mao, C.; Solis, D. J.; Ryan, K. S.; Thomson, T.; Belcher, A. M. Biological Routes to Metal Alloy Ferromagnetic Nanostructures. *Nano Lett.* **2004**, *4*, 1127–1132.
16. Rosant, C.; Avalle, B.; Larcher, D.; Dupont, L.; Friboulet, A.; Tarascon, J.-M. Biosynthesis of Co_3O_4 Electrode Materials by Peptide and Phage Engineering: Comprehension and Future. *Energy Environ. Sci.* **2012**, *5*, 9936–9943.
17. Kashyap, S.; Woehl, T. J.; Liu, X.; Mallapragada, S. K.; Prozorov, T. Nucleation of Iron Oxide Nanoparticles Mediated by Mms6 Protein *in Situ*. *ACS Nano* **2014**, *8*, 9097–9106.
18. Jeong, C. K.; Kim, I.; Park, K.-I.; Oh, M. H.; Paik, H.; Hwang, G.-T.; No, K.; Nam, Y. S.; Lee, K. J. Virus-Directed Design of a Flexible $BaTiO_3$ Nanogenerator. *ACS Nano* **2013**, *7*, 11016–11025.
19. Nam, K. T.; Kim, D.-W.; Yoo, P. J.; Chiang, C.-Y.; Meethong, N.; Hammond, P. T.; Chiang, Y.-M.; Belcher, A. M. Virus-Enabled Synthesis and Assembly of Nanowires for Lithium Ion Battery Electrodes. *Science* **2006**, *312*, 885–888.
20. Lee, Y. J.; Yi, H.; Kim, W.-J.; Kang, K.; Yun, D. S.; Strano, M. S.; Ceder, G.; Belcher, A. M. Fabricating Genetically Engineered High-Power Lithium-Ion Batteries Using Multiple Virus Genes. *Science* **2009**, *324*, 1051–1055.
21. Rui, X.; Yan, Q.; Skyllas-Kazacos, M.; Lim, T. M. $Li_3V_2(PO_4)_3$ Cathode Materials for Lithium-Ion Batteries: A Review. *J. Power Sources* **2014**, *258*, 19–38.
22. Rui, X.; Sim, D.; Wong, K.; Zhu, J.; Liu, W.; Xu, C.; Tan, H.; Xiao, N.; Hng, H. H.; Lim, T. M. $Li_3V_2(PO_4)_3$ Nanocrystals Embedded in a Nanoporous Carbon Matrix Supported on Reduced Graphene Oxide Sheets: Binder-Free and High Rate Cathode Material for Lithium-Ion Batteries. *J. Power Sources* **2012**, *214*, 171–177.
23. Jian, Z.; Han, W.; Lu, X.; Yang, H.; Hu, Y. S.; Zhou, J.; Zhou, Z.; Li, J.; Chen, W.; Chen, D. Superior Electrochemical Performance and Storage Mechanism of $Na_3V_2(PO_4)_3$ Cathode for Room-Temperature Sodium-Ion Batteries. *Adv. Energy Mater.* **2013**, *3*, 156–160.
24. Zhu, C.; Song, K.; van Aken, P. A.; Maier, J.; Yu, Y. Carbon-Coated $Na_3V_2(PO_4)_3$ Embedded in Porous Carbon Matrix: An Ultrafast Na-Storage Cathode with the Potential of Outperforming Li Cathodes. *Nano Lett.* **2014**, *14*, 2175–2180.
25. Li, S.; Dong, Y.; Xu, L.; Xu, X.; He, L.; Mai, L. Effect of Carbon Matrix Dimensions on the Electrochemical Properties of $Na_3V_2(PO_4)_3$ Nanograins for High-Performance Symmetric Sodium-Ion Batteries. *Adv. Mater.* **2014**, *26*, 3545–3553.
26. Nettles, D. L.; Chilkoti, A.; Setton, L. A. Applications of Elastin-Like Polypeptides in Tissue Engineering. *Adv. Drug Delivery Rev.* **2010**, *62*, 1479–1485.
27. Cho, Y.; Zhang, Y.; Christensen, T.; Sagle, L. B.; Chilkoti, A.; Cremer, P. S. Effects of Hofmeister Anions on the Phase Transition Temperature of Elastin-Like Polypeptides. *J. Phys. Chem. B* **2008**, *112*, 13765–13771.

28. Connor, P.; McQuillan, A. J. Phosphate Adsorption onto TiO_2 from Aqueous Solutions: An *in Situ* Internal Reflection Infrared Spectroscopic Study. *Langmuir* **1999**, *15*, 2916–2921.
29. Kótai, L.; Sajó, I. E.; May, Z.; Gács, I.; Fodor, J. A Convenient Method to Prepare Alkali-and Chloride-Free Ammonium Metavanadate (NH_4VO_3). *Chem. Lett.* **2006**, *35*, 384–385.
30. Osante, I.; Polo, E.; Revilla-López, G.; Jesús, M.; Alemán, C.; Cativiela, C.; Díaz, D. D. α-Alkyl Cysteine-Coated Gold Nanoparticles: Effect of Cα-Tetrasubstitution on Colloidal Stability. *J. Nanopart. Res.* **2014**, *16*, 1–12.
31. Kang, K.; Meng, Y. S.; Bréger, J.; Grey, C. P.; Ceder, G. Electrodes with High Power and High Capacity for Rechargeable Lithium Batteries. *Science* **2006**, *311*, 977–980.
32. Wu, X. L.; Jiang, L. Y.; Cao, F. F.; Guo, Y. G.; Wan, L. J. $LiFePO_4$ Nanoparticles Embedded in a Nanoporous Carbon Matrix: Superior Cathode Material for Electrochemical Energy-Storage Devices. *Adv. Mater.* **2009**, *21*, 2710–2714.
33. Wang, L.; Zhang, L.-C.; Lieberwirth, I.; Xu, H.-W.; Chen, C.-H. A $Li_3V_2(PO_4)_3$/C Thin Film with High Rate Capability as a Cathode Material for Lithium-Ion Batteries. *Electrochem. Commun.* **2010**, *12*, 52–55.
34. Yuan, D.; Liang, X.; Wu, L.; Cao, Y.; Ai, X.; Feng, J.; Yang, H. A Honeycomb-Layered $Na_3Ni_2SbO_6$: A High-Rate and Cycle-Stable Cathode for Sodium-Ion Batteries. *Adv. Mater.* **2014**, *26*, 6301–6306.
35. Jung, Y. H.; Lim, C. H.; Kim, D. K. Graphene-Supported $Na_3V_2(PO_4)_3$ as a High Rate Cathode Material for Sodium-Ion Batteries. *J. Mater. Chem. A* **2013**, *1*, 11350–11354.
36. Rui, X.; Ding, N.; Liu, J.; Li, C.; Chen, C. Analysis of the Chemical Diffusion Coefficient of Lithium Ions in $Li_3V_2(PO_4)_3$ Cathode Material. *Electrochim. Acta* **2010**, *55*, 2384–2390.
37. Song, W.; Ji, X.; Wu, Z.; Zhu, Y.; Yang, Y.; Chen, J.; Jing, M.; Li, F.; Banks, C. E. First Exploration of Na-Ion Migration Pathways in the NASICON Structure $Na_3V_2(PO_4)_3$. *J. Mater. Chem. A* **2014**, *2*, 5358–5362.
38. Tjin, M. S.; Chua, A. W. C.; Ma, D. R.; Lee, S. T.; Fong, E. Human Epidermal Keratinocyte Cell Response on Integrin-Specific Artificial Extracellular Matrix Proteins. *Macromol. Biosci.* **2014**, *14*, 1125–1134.